

Search for continuous gravitational waves from Fomalhaut b in the second Advanced LIGO observing run with a hidden Markov model

Dana Jones¹ and Ling Sun^{2,3}

¹*College of Arts and Sciences, University of Pennsylvania, Philadelphia, Pennsylvania 19104, USA*

²*LIGO Laboratory, California Institute of Technology, Pasadena, California 91125, USA*

³*OzGrav, ANU Centre for Gravitational Astrophysics,
Research Schools of Physics, and Astronomy and Astrophysics,
The Australian National University, Canberra, 2601, Australia*

(Dated: October 29, 2021)

Results are presented from a semicoherent search for continuous gravitational waves from a nearby neutron star candidate, Fomalhaut b, using data collected in the second observing run of Advanced LIGO. The search is based on a hidden Markov model scheme, capable of tracking signal frequency evolution from the star’s secular spin down and stochastic timing noise simultaneously. The scheme is combined with a frequency domain matched filter (\mathcal{F} -statistic), calculated coherently over five-day time stretches. The frequency band 100–1000 Hz is searched. After passing the above-threshold candidates through a hierarchy of vetoes, one candidate slightly above the 1% false alarm probability threshold remains for further scrutiny. No strong evidence of continuous waves is found. We present the frequentist strain upper limits at 95% confidence.

I. INTRODUCTION

Gravitational waves (GWs), perturbations in spacetime that propagate at the speed of light, were first directly observed in 2015 when the Advanced Laser Interferometer Gravitational-Wave Observatory (Advanced LIGO) detected a merging binary black hole system (GW150914) [1, 2]. The Virgo detector joined the observation at the end of the second observing run (O2) in 2017 [3]. In the years since the first detection, the sensitivity of these interferometers has been greatly improved, allowing for increasingly frequent detections of compact binary coalescences (CBCs) [4–7]. Other types of GW sources that also radiate at frequencies within the observational band of ground-based interferometers remain yet-undetected, e.g., the persistent, well modelled, continuous gravitational waves (CWs) produced by isolated spinning neutron stars. These CWs, if detected, will provide invaluable information regarding the structure of the neutron stars as well as the nuclear equation of state in extreme-pressure situations [8]. A great deal of work has been carried out to develop methods and conduct searches for CWs. There are three main types of CW searches: (1) targeted searches for pulsars whose sky positions and ephemerides are well measured electromagnetically (e.g., [9, 10]), (2) directed searches for neutron stars with known sky positions but unknown rotation frequencies (e.g., [11–14]), and (3) all-sky searches, surveys done over the whole sky to search for emitting sources (e.g., [15]).

In this paper, a directed search, more expensive than a targeted search but less expensive than an all-sky search, is conducted in the Advanced LIGO O2 data [16] for a nearby neutron star candidate, Fomalhaut b. Fomalhaut b was originally hypothesized to be an exoplanet orbiting around the star Fomalhaut A [17, 18]. However, certain peculiarities, namely its non-detection in the infrared and its potentially highly eccentric orbit, have led to specu-

lation over whether or not it is in fact an exoplanet. A different hypothesis has been gaining momentum; rather than a companion object, Fomalhaut b may in fact be a background neutron star to Fomalhaut A [19]. There has also been recent evidence that Fomalhaut b may be a directly imaged catastrophic collision between two large planetesimals in an extrasolar planetary system [20]. Although the remaining uncertainty regarding the source’s identity may make it a less promising candidate for a CW search, Fomalhaut b remains of interest due to its extremely close proximity. It is currently hypothesised to be just 11 pc away, which would make it, assuming the neutron star hypothesis to be true, the closest known neutron star to our solar system [19]. A CW search directed at Fomalhaut b was conducted in the first observing run of Advanced LIGO, but no evidence of gravitational radiation was found [12].

Since the expected strain amplitudes of CWs are orders of magnitude smaller than those produced by CBCs, vast computational resources are required to integrate observational data coherently over a long period of time (e.g., ~ 1 yr), searching for the signal frequency and the time derivatives [8]. In addition, intrinsic, stochastic frequency wandering, or “timing noise,” associated with the secular spin down of a star could degrade the sensitivity of a fully coherent search [21]. Thus, although fully coherent searches are still of interest in certain systems with negligible timing noise, we conduct a computationally efficient semicoherent search based on a hidden Markov model (HMM) scheme, equipped to track the evolving signal frequency due to secular spin down and stochastic timing noise [22]. The tracking scheme has its origins in engineering, and has recently been used in many CW searches (e.g., [11, 14, 23–25]).

The search presented in this paper is conducted using the Advanced LIGO O2 data collected from January 3 to August 25, 2017 in the frequency band 100–1000 Hz, divided into 1-Hz sub-bands to parallelize the computation.

The total observing duration is split into five-day coherent segments in order to balance search sensitivity and computing cost in the presence of timing noise. The short Fourier transforms (SFTs) of the data are passed through a frequency domain matched filter (the \mathcal{F} -statistic). These coherent five-day segments are combined incoherently using a HMM tracking scheme. The search output is then passed through a hierarchy of veto validations. No strong evidence of continuous waves is found.

The organization of the paper is as follows. Section II outlines the methods used in the search. Section III details the search setup, including source parameters, search configuration, threshold, and sensitivity estimates. In Section IV, we explain the results from the search, including the five vetoes applied to the over-threshold candidates, and discuss future work that could be used to further follow up on the results. Finally, the conclusion is given in Section V.

II. METHODS

This search is composed of two main procedures: (1) coherently summing up the signal power over consecutive five-day time stretches using the \mathcal{F} -statistic, and (2) a HMM tracking to find the most probable signal evolution path over the total observing run. The signal model is briefly reviewed in Section II A. The two procedures are described in Sections II B and II C, respectively. The detection statistic adopted in this search, the Viterbi score, is defined in Section II D.

A. Signal model

The phase of the signal as observed in the detector can be described as [26]

$$\Phi(t) = 2\pi \sum_{k=0}^s \frac{f_0^{(k)} t^{k+1}}{(k+1)!} + \frac{2\pi}{c} \hat{n} \cdot \vec{r}(t) \sum_{k=0}^s \frac{f_0^{(k)} t^k}{k!}, \quad (1)$$

where f_0 is the signal frequency at reference time $t = 0$, the superscript (k) denotes the k th time derivative of the signal frequency, \hat{n} is the unit vector directed outward from the solar system barycenter (SSB) to the neutron star, and $\vec{r}(t)$ is the position vector of the detector relative to the SSB. Then, the signal can be expressed as

$$h(t) = \mathcal{A}^\mu h_\mu(t), \quad (2)$$

where \mathcal{A}^μ , depending on the phase in (1), characteristic gravitational-wave strain amplitude h_0 , and source orientation, represents the amplitudes associated with the four linearly independent components $h_\mu(t)$. (See full description in Refs. [22, 26].)

B. \mathcal{F} -statistic

The \mathcal{F} -statistic is a matched filter used to estimate the likelihood that a signal described above is present in the frequency domain. The time-domain data $x(t)$ collected by the detector can be written as

$$x(t) = \mathcal{A}^\mu h_\mu(t) + n(t) \quad (3)$$

where $n(t)$ is stationary, additive noise [26]. First, a scalar product as a sum over single-detector inner products is defined as

$$(x|y) = \sum_X (x^X|y^X) \quad (4)$$

$$= \sum_X 4\Re \int_0^\infty df \frac{\tilde{x}^X(f) \tilde{y}^{X*}(f)}{S_h^X(f)}, \quad (5)$$

where X indexes the detector, $S_h^X(f)$ is the single-sided power spectral density (PSD) of detector X , the tilde denotes a Fourier transform, and \Re is the real part of a complex number [27]. Then, the \mathcal{F} -statistic can be written in the form

$$\mathcal{F} = \frac{1}{2} x_\mu \mathcal{M}^{\mu\nu} x_\nu, \quad (6)$$

where $x_\mu = (x|h_\mu)$, and $\mathcal{M}^{\mu\nu}$ represents the matrix inverse of $\mathcal{M}_{\mu\nu} = (h_\mu|h_\nu)$ [22]. If the noise is Gaussian and the single-sided PSD is the same in all detectors, the probability of having a signal in the data solely depends the signal-to-noise ratio, given by [26]

$$\rho_0^2 = \frac{K h_0^2 T_{\text{coh}}}{S_h(f)}, \quad (7)$$

where K is a constant that depends on the sky location, orientation of the source, and number of detectors, and T_{coh} is the length of data combined coherently.

C. Hidden Markov model

This semicoherent search, based on the HMM scheme, is solved by the Viterbi algorithm to identify the most likely frequency evolution path of the signal. (See Ref. [28] for an explanation of the classic Viterbi algorithm.) It is computationally efficient and robust in the presence of timing noise [22].

A Markov chain is a stochastic process that transitions from one discrete state to another at discrete times. A hidden Markov model is comprised of two variables: the unobservable, hidden state variable $q(t) \in \{q_1, \dots, q_{N_Q}\}$ and the observable, measurement state variable $o(t) \in \{o_1, \dots, o_{N_O}\}$, where N_Q and N_O are the total number of hidden and measurement states, respectively. For any time t_{n+1} , the hidden state is solely dependent on the state at time t_n and has a transition probability of

$$A_{q_j q_i} = \Pr[q(t_{n+1}) = q_j | q(t_n) = q_i]. \quad (8)$$

The hidden state q_i , present in the observable state o_j , has an emission probability defined as

$$L_{o_j q_i} = \Pr[o(t_n) = o_j | q(t_n) = q_i], \quad (9)$$

at time t_n . The prior is written as

$$\Pi_{q_i} = \Pr[q(t_1) = q_i], \quad (10)$$

where t_1 is the reference time of the first time step. The probability that an observed sequence $O = o(t_1), \dots, o(t_{N_T})$, where N_T is the total number of time steps, is the result of a hidden state path $Q = q(t_1), \dots, q(t_{N_T})$ via a Markov chain can be described by

$$\begin{aligned} \Pr(Q|O) = & L_{o(t_{N_T})q(t_{N_T})} A_{q(t_{N_T})q(t_{N_T-1})} \cdots L_{o(t_2)q(t_2)} \\ & \times A_{q(t_2)q(t_1)} \Pi_{q(t_1)}. \end{aligned} \quad (11)$$

The most probable path, calculated by maximizing $\Pr(Q|O)$ is [22]

$$Q^*(O) = \arg \max \Pr(Q|O), \quad (12)$$

where $\arg \max(\dots)$ returns the argument that maximizes (\dots) .

In this search, the one-dimensional state variable $q(t)$ is defined as $f_0(t)$. The discrete hidden states are mapped one-to-one to the frequency bins that make up the output of $\mathcal{F}(f)$ calculated over the span of length T_{coh} (see Section II B). Each frequency bin size is then $\Delta f = 1/(2T_{\text{coh}})$. We choose T_{coh} to satisfy

$$\left| \int_t^{t+T_{\text{coh}}} dt' \dot{f}_0(t') \right| < \Delta f \quad (13)$$

for $0 < t < T_{\text{obs}} - T_{\text{coh}}$, where T_{obs} is the total observation time. (See Ref. [22] for more details).

Assuming that the frequency evolution caused by timing noise is much slower than that due to secular spin down, and $|\dot{f}_0|$ follows a uniform distribution between zero and the maximum estimated frequency derivative $|\dot{f}_0|_{\text{max}}$, we can substitute $|\dot{f}_0|_{\text{max}}$ into (13) and simplify (8) to become

$$A_{q_{i-1}q_i} = A_{q_i q_i} = \frac{1}{2}, \quad (14)$$

with all other $A_{q_j q_i}$ entries vanishing. Then, using the definition of \mathcal{F} -statistic, the emission probability is defined as

$$L_{o(t)q_i} = \Pr[o(t) | f_i \leq f_0(t) \leq f_i + \Delta f] \quad (15)$$

$$\propto \exp[\mathcal{F}(f_i)], \quad (16)$$

from t to $t+T_{\text{coh}}$, where f_i represents the central frequency in the i th bin. A uniform prior of $\Pi_{q_i} = N_Q^{-1}$ is selected because there is no independent knowledge of f_0 [22].

The algorithm outputs the most likely frequency evolution path $Q^*(O)$ over the course of T_{obs} . This is called the Viterbi path and consists of a frequency estimated

at each discrete time step. Figure 1 shows an example of tracking a circularly polarized synthetic signal with $h_0 = 1.57 \times 10^{-26}$ and $\cos \iota = 1$, where ι is the source inclination angle, starting at $f_0 = 155.3$ Hz (a frequency chosen randomly), and injected into Gaussian noise with amplitude spectral density (ASD) $S_h^{1/2} = 4 \times 10^{-24} \text{ Hz}^{-1/2}$. The total observing time tracked is 234 days, with $T_{\text{coh}} = 5$ d. The first and second time derivatives of the injected signal frequency are $\dot{f}_0 = -2 \times 10^{-12} \text{ Hz s}^{-1}$ and $\ddot{f}_0 = 2 \times 10^{-24} \text{ Hz s}^{-2}$. The optimal signal evolution path reconstructed by the Viterbi algorithm (red) is plotted over the injected signal path (blue). The reconstructed path shows a stair-step pattern because the HMM method uses discrete frequency bins (shown as dashed lines). The injected signal, by contrast, evolves continuously. The recovered path matches the injected signal well in that it never strays more than two bins from the true frequency. The root-mean-square error between the two paths is $7.8 \times 10^{-7} \text{ Hz}$, smaller than the discrete bin size, $1.16 \times 10^{-6} \text{ Hz}$.

D. Viterbi score

We follow the existing literature and define Viterbi score to evaluate the significance of any candidate output from the search [22, 23]. In each sub-band searched (with width 1 Hz in this paper), the Viterbi score S is defined such that the log likelihood of the optimal Viterbi path is equal to the mean log likelihood of all paths ending in different bins of the sub-band plus S standard deviations at final step N_T . This is shown as follows:

$$S = \frac{\ln \delta_{q^*}(t_{N_T}) - \mu_{\ln \delta}(t_{N_T})}{\sigma_{\ln \delta}(t_{N_T})} \quad (17)$$

where

$$\mu_{\ln \delta}(t_{N_T}) = N_Q^{-1} \sum_{i=1}^{N_Q} \ln \delta_{q_i}(t_{N_T}) \quad (18)$$

and

$$\sigma_{\ln \delta}(t_{N_T})^2 = N_Q^{-1} \sum_{i=1}^{N_Q} [\ln \delta_{q_i}(t_{N_T}) - \mu_{\ln \delta}(t_{N_T})]^2. \quad (19)$$

Here, $\delta_{q_i}(t_{N_T})$ is the maximum probability of the path that ends in state q_i ($1 \leq i \leq N_Q$) at step N_T , and $\delta_{q^*}(t_{N_T})$ is the likelihood of the optimal Viterbi path (i.e., the probability $\Pr[Q^*(O)|O]$). The higher the score S , the more likely that a signal is present in the sub-band.

III. SEARCH SETUP

In this section, we first discuss the source parameters and the parameter space covered in the search in Section III A. Sections III B and III C describe the detection threshold and estimated search sensitivity, respectively.

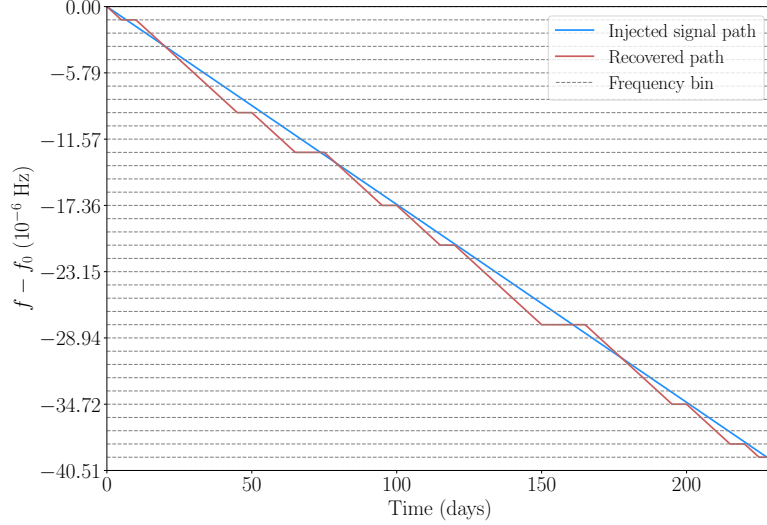


FIG. 1. HMM tracking of a synthetic signal with $h_0 = 1.57 \times 10^{-26}$ and $\cos \iota = 1$, injected into Gaussian noise (ASD $S_h^{1/2} = 4 \times 10^{-24} \text{ Hz}^{-1/2}$) at a starting frequency of 155.3 Hz. The blue curve represents the injected signal (with $\dot{f}_0 = -2 \times 10^{-12} \text{ Hz s}^{-1}$ and $\ddot{f}_0 = 2 \times 10^{-24} \text{ Hz s}^{-2}$), and the red curve represents the optimal Viterbi path recovered by the HMM tracking. The dashed lines indicate the size of the discrete frequency bins.

A. Source parameters and search configuration

Fomalhaut b is located at right ascension 22 h 57 m 39.1 s and declination $29^\circ 37' 20.0''$ (J2000). Ref. [12] considered both the most optimistic and pessimistic estimates of Fomalhaut b's distance (0.011–0.02 kpc) and age (316–3000 kpyr) in the literature.

Here, we mainly rely on the estimated, age-based spin-down rate in order to choose an optimal T_{coh} in this search. The age-based \dot{f}_0 is estimated using [12, 22]

$$-\frac{\dot{f}_0}{(n_{\min} - 1)t_{\text{age}}} \leq \dot{f}_0 \leq -\frac{\dot{f}_0}{(n_{\max} - 1)t_{\text{age}}}, \quad (20)$$

where t_{age} is the age of the source, and n_{\min} and n_{\max} , respectively, represent the minimum and maximum values of the breaking index $n = f_0 \dot{f}_0 / \dot{f}_0^2$. Given an estimated \dot{f}_0 , a T_{coh} value may then be chosen based on the following equation:

$$T_{\text{coh}} \leq (2|\dot{f}_0|)^{-1/2}, \quad (21)$$

such that (13) is satisfied. Since the search sensitivity improves as T_{coh} increases for a given T_{obs} [22], we usually set $T_{\text{coh}} = (2|\dot{f}_0|)^{-1/2}$.

The frequency range searched in this analysis is 100–1000 Hz, where the Advanced LIGO detectors are most sensitive. Table I lists the $|\dot{f}_0|$ ranges calculated using (20), and the corresponding T_{coh} ranges calculated using (21), for $f_0 \in [100, 1000] \text{ Hz}$. The ranges are calculated for each $n \in \{2, 5, 7\}$ and $t_{\text{age}} \in \{316, 3000\} \text{ kyr}$. Since the uncertainty of the estimated t_{age} is large, we select an

n	t_{age} (kyr)	$ \dot{f}_0 $ (Hz s $^{-1}$)	T_{coh} (days)
2	316	$[1.00 \times 10^{-11}, 1.00 \times 10^{-10}]$	[0.82, 2.58]
2	3000	$[1.06 \times 10^{-12}, 1.06 \times 10^{-11}]$	[2.52, 7.96]
5	316	$[2.51 \times 10^{-12}, 2.51 \times 10^{-11}]$	[1.63, 5.17]
5	3000	$[2.64 \times 10^{-13}, 2.64 \times 10^{-12}]$	[5.03, 15.92]
7	316	$[1.67 \times 10^{-12}, 1.67 \times 10^{-11}]$	[2.00, 6.33]
7	3000	$[1.76 \times 10^{-13}, 1.76 \times 10^{-12}]$	[6.17, 19.50]

TABLE I. Estimated ranges of $|\dot{f}_0|$ and T_{coh} . The frequency range considered is 100–1000 Hz.

intermediate $T_{\text{coh}} = 5 \text{ d}$, corresponding to a \dot{f}_0 range of $\dot{f}_0 \in [-2.68 \times 10^{-12}, 0] \text{ Hz s}^{-1}$. With this choice of T_{coh} , the search can cover most of the interesting parameter space, if the torque is dominated by gravitational radiation reaction ($n = 5$) or r -mode oscillations ($n = 7$), e.g., almost the full 100–1000 Hz band if $t_{\text{age}} \sim 10^3 \text{ kyr}$, or the most sensitive hundred-hertz band if $t_{\text{age}} \sim 10^2 \text{ kyr}$. Signals with \dot{f}_0 out of the covered range during part of the observing run could still be partially tracked by the HMM. The desired sensitivity of the search (Section III C), however, cannot be achieved. Note that although the minimum $T_{\text{coh}} = 0.82 \text{ d}$ in Table I could cover all scenarios listed above, it is not the optimal choice since the sensitivity degrades as T_{coh} decreases ($\propto T_{\text{coh}}^{-1/4}$) [22].

The total observation period searched is the duration of Advanced LIGO's O2 run, excluding the first few

weeks when the data quality was not optimal and was followed by a brief end-of-the-year break; that is, GPS time 1167545066–1187733592 (January 3 to August 25, 2017), a total duration of about 234 days. Given the chosen $T_{\text{coh}} = 5$ d, we have the total number of steps $N_T = 47$.

B. Threshold

The Viterbi score threshold S_{th} , corresponding to a desired false alarm probability α_f in each sub-band ($\alpha_f = 1\%$ in this search), is determined through Gaussian noise simulations. In each of the five sample 1-Hz sub-bands, starting from 100 Hz, 300 Hz, 500 Hz, 700 Hz, and 900 Hz, 200 realizations of pure Gaussian noise are generated and searched with the same configuration as used in the real search (i.e., $T_{\text{coh}} = 5$ d and $T_{\text{obs}} = 234$ d). The resulting 1000 scores are sorted and then the score at the 99th percentile is determined as the threshold, $S_{\text{th}} = 6.95$. Ten out of the 1000 scores obtained from pure noise are above S_{th} , corresponding to $\alpha_f = 1\%$ per 1-Hz sub-band.

This threshold is verified using O2 interferometric data. In three clean 1-Hz sub-bands, starting from 300 Hz, 600 Hz, and 900 Hz, 200 noise-only realizations are simulated by drawing random sky positions. The total 600 realizations yield a threshold $S_{\text{th}} = 6.97$ ($\alpha_f = 1\%$ per 1-Hz sub-band), in good agreement with the threshold obtained in pure Gaussian noise. Hence we set $S_{\text{th}} = 6.95$ in this search.

C. Sensitivity

We evaluate the search sensitivity by quantifying the h_0 value required to achieve a 95% detection efficiency, denoted by $h_0^{95\%}$. It is first obtained by injecting 100 synthetic signals with a fixed h_0 value into Gaussian noise ($\text{ASD } S_h^{1/2} = 4 \times 10^{-24} \text{ Hz}^{-1/2}$) in four 1-Hz sub-bands, starting from 155 Hz, 355 Hz, 555 Hz, and 755 Hz. These simulations are marginalized over the orientation of the source, with the sky location fixed at the true position of Fomalhaut b. If more than 95% of the signals are correctly recovered, this process is repeated with a smaller value of h_0 , and vice versa. We obtain an average of $h_0^{95\%} = 3.91 \times 10^{-26}$ in these four sub-bands.

This process is repeated in O2 interferometric data in a sample 1-Hz sub-band starting from 715 Hz, randomly chosen from among the relatively clean bands. We obtain $h_0^{95\%} = 1.67 \times 10^{-25}$, an order of magnitude larger than $h_0^{95\%}$ obtained in Gaussian noise. This is because (1) the O2 noise ASD has not reached the design sensitivity of Advanced LIGO, and (2) the duty cycle (i.e., the proportion of time that the data is in analyzable science mode) of O2 is only about 50%. The sensitivity in the full frequency band is presented in Sec. IV B and interpreted as the upper limits on h_0 .

IV. RESULTS

In this section, we describe the first-pass candidates obtained from the analysis with $S > S_{\text{th}}$, and a series of vetoes validating these candidates in Section IV A. After the veto procedure, only one candidate (with Viterbi score slightly above threshold) remains for further scrutiny. Without strong evidence of CW, we present the strain upper limits and astrophysical interpretation in Section IV B.

A. Candidates and vetoes

We find in total 160 first-pass candidates with $S > S_{\text{th}}$. A large portion of the first-pass candidates are contributed from noise artifacts and the non-Gaussianity in the interferometric data. Narrow-band noise lines, e.g., 60 Hz power line harmonics, thermally excited mirror suspension violin modes, and lines from environmental disturbances are all sources of noise artifacts that obscure astrophysical CW signals. A five-step veto process is conducted to eliminate candidates resulting from noise artifacts [23]. See Table II for the number of candidates remaining after each step. See Figure 2 for all the candidates with their Viterbi scores plotted as a function of frequency, as well as at which step each candidate is vetoed. The detailed veto criteria are described as follows.

Processing step	Candidates Remaining
First pass	160
Know-line veto	96
Single-interferometer veto	13
$T_{\text{obs}}/2$ veto	10
Double T_{coh} veto	6
Off-target veto	1

TABLE II. Number of candidates remaining after each processing step. In total 160 first-pass candidates are found with $S > S_{\text{th}} = 6.95$. After the five veto steps, one candidate remains for further scrutiny.

First, we take into account the maximum Doppler shift due to the Earth's motion, $\delta f \approx 10^{-4} f_0$ (here f_0 is the starting frequency of the path), and widen the Viterbi path of each candidate by δf on both sides of the path. We eliminate 64 candidates whose widened Viterbi paths intersect any known instrumental lines present in either the Hanford or Livingston interferometer [29, 30].

Second, an additional 83 candidates are vetoed due to the contamination from not well understood artifacts in a single detector. The criteria are as follows. For each candidate, if searching data from a single interferometer yields $S \geq S_{\cup}$, where S_{\cup} is the original score obtained with both interferometers combined, while searching the other interferometer yields $S < S_{\text{th}}$, and if the Viterbi path from the interferometer with $S \geq S_{\cup}$ intersects the

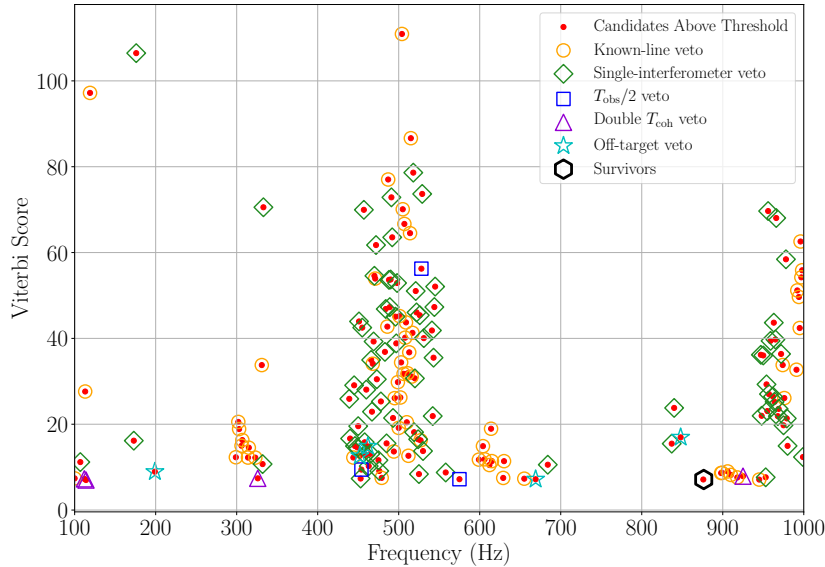


FIG. 2. Viterbi score S of the first-pass candidate in each 1-Hz sub-band as a function of frequency (red dots). Candidates marked by orange circles, green diamonds, blue squares, purple triangles, and cyan stars are eliminated in stages 1–5 of the veto procedure (see Section IV A for details of the veto criteria). The only surviving candidate is marked by a black hexagon.

original path, that candidate is vetoed. We eliminate 49 more candidates here. The above criterion is a stringent consistency check. After manually checking the remaining candidates, we find that a large portion of them are also caused by artifacts in a single detector, but do not necessarily meet the stringent criterion above. We inspect the candidate scores and paths manually and veto an additional 34 candidates due to contamination from a single detector. They fall into one of the three special cases: (a) We have $S > S_U \gg S_{th}$ in one detector and $S < S_{th}$ in the other, i.e., the candidate power completely comes from a single detector. The Viterbi path from the interferometer with $S \geq S_U$ does not intersect the original path (hence not automatically vetoed), but the two paths only differ by $\lesssim 0.02$ Hz. (b) We have a larger $S > S_U \gg S_{th}$ in one detector, but in the other we have S slightly above S_{th} (hence not automatically vetoed). The Viterbi path from the detector with $S > S_U$ intersects the original path, and the Viterbi path from the detector with $S \sim S_{th}$ does not intersect the original path. In addition, the higher S from one detector is at least a number of 40 larger than S from the other. (c) We have $S \sim S_U \gg S_{th}$ in one detector (S slightly below S_U , hence not automatically vetoed) and $S < S_{th}$ in the other. The Viterbi path from the detector with larger S intersects the original path. In this case, the candidate is so loud that the Viterbi score is saturated around $S_U \gtrsim 50 \gg S_{th}$.

Third, an additional three candidates are vetoed by splitting the observation time into two halves and analyzing each half separately. A candidate is vetoed if the

score obtained by searching one half of T_{obs} is higher than or equal to S_U (corresponding to the full T_{obs}), while the score obtained in the other half is lower than S_{th} , and if the Viterbi path from the half with the higher score intersects the original path.

Fourth, the remaining ten candidates are further followed up by increasing T_{coh} . We increase T_{coh} from five to ten days for a candidate whose estimated mean f_0 over T_{obs} is small enough such that Equation (21) holds true when $T_{coh} = 10$ d. Then, for each candidate, the \mathcal{F} -statistic and the Viterbi path are recomputed, using both interferometers combined. If the candidate is from astrophysical origin, the resulting Viterbi score with $T_{coh} = 10$ d should be higher than S_U , and the output Viterbi paths from searches with $T_{coh} = 5$ d and 10 d should match. Hence we veto a candidate if its score corresponding to $T_{coh} = 10$ d falls below S_U and if the Viterbi paths from these two separate searches are at least 0.01 Hz apart. The candidate in the 462 Hz sub-band is excluded from this procedure because its estimated mean f_0 is so large that (21) is no longer satisfied if we increase T_{coh} to 10 d. We eliminate four candidates in this step.

Fifth, all but one candidate is eliminated using an “off-target” veto. For each of the remaining six candidates, we first shift the sky location by increasing the right ascension by offsets ranging from 10 sec to 1 hr from the source’s true location, with the declination fixed. We then increase the declination by offsets ranging from 10 sec to 1 deg from the source’s true location, with the right ascension fixed at the true value. We conduct the search and obtain

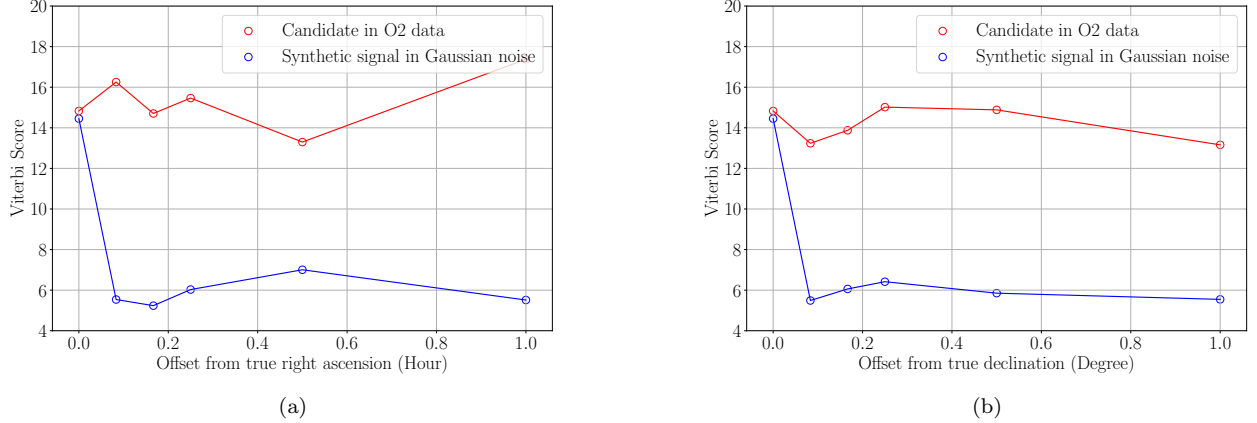


FIG. 3. Viterbi score as a function of the (a) right ascension and (b) declination offsets in the 1-Hz sub-band starting at 462 Hz. The red and blue curves show the results obtained when following up the candidate in the real data and an injection in Gaussian noise, respectively. The results obtained for the candidate in real data show a steady and even increasing score as the offset increases. The simulation shows that the score drops below S_{th} within $\sim 5'$ from the true location (either for right ascension or declination). This candidate can therefore be vetoed.

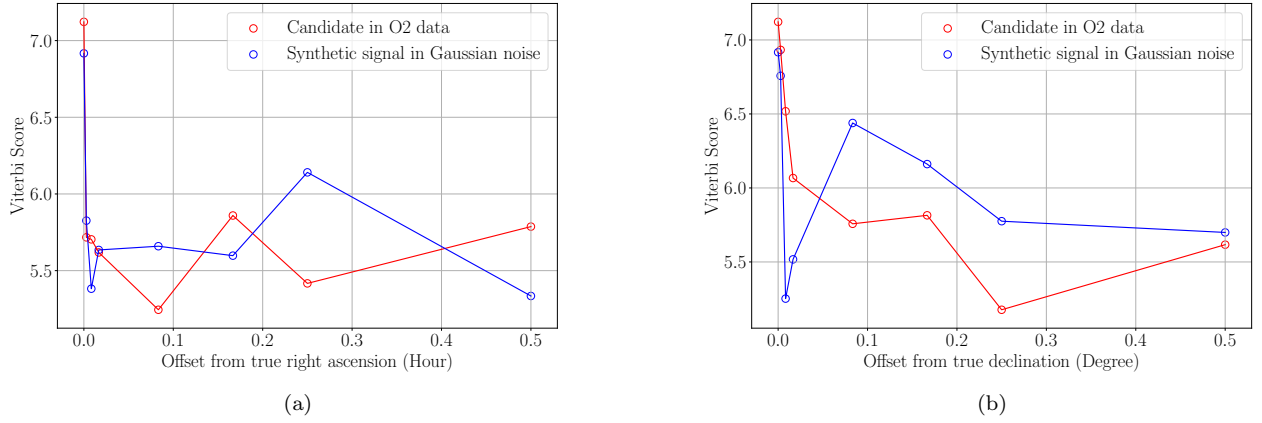


FIG. 4. Viterbi score as a function of the (a) right ascension and (b) declination offsets in the 1-Hz sub-band starting at 876 Hz. The red and blue curves show the results obtained when following up the candidate in the real data and an injection in Gaussian noise, respectively. Both the scores obtained for the candidate in real data and the injection drop below threshold within $\sim 30''$ from the true location. The candidate survives this veto.

the Viterbi score for each off-target position. A candidate is vetoed if this series of searches targeting sky locations shifted from the source's true location do not continuously yield Viterbi scores lower than the original score. That is, if the score does not drop below the threshold as we move away from the source's true location, we veto the candidate. The reliability of this veto is verified through synthetic signals injected into Gaussian noise. The same series of searches targeting the true sky location of the injection as well as the off-target locations is conducted. The simulation results demonstrate that the score drops below S_{th} as we move away from the true sky location of the injection with an offset of $\sim 5'$ in either right ascension

or declination. A sample in the 462–463 Hz sub-band, which corresponds to a vetoed candidate in this step, is shown in Figure 3.

The only candidate that survives the off-target veto is in the 876–877 Hz sub-band. The off-target search results in the real data in this sub-band behave exactly like those obtained from the simulations, as shown in Figure 4. The Viterbi score immediately drops as we move away from the source's true location. The scores remain below threshold as we continue to increase the offset. Since this candidate behaves like an astrophysical signal, we keep it for further scrutiny.

Finally, the single remaining candidate in the 1-Hz

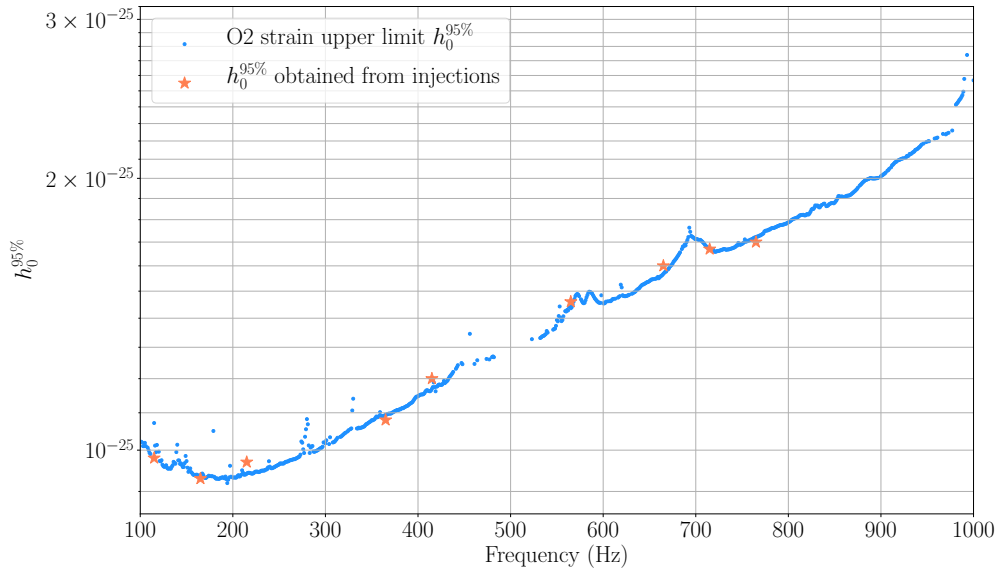


FIG. 5. The frequentist strain upper limits at 95% confidence level, $h_0^{95\%}$, as a function of frequency. The blue dots represent the estimated $h_0^{95\%}$ in the full band, and the orange stars represent the nine sample 1-Hz sub-bands where the $h_0^{95\%}$ values were obtained empirically. The sub-bands without a marker were vetoed.

sub-band starting at 876 Hz (path starts at $f_0 = 876.5034513780022$ Hz) is followed up using a technique in which the Doppler modulation, which accounts for the Doppler shift due to Earth's motion, is turned off when computing \mathcal{F} -statistic [31], and the Viterbi score is recomputed. A signal of astrophysical origin usually becomes undetectable and a different Viterbi path is returned when turning the Doppler modulation off. However, a candidate caused by noise artifacts should yield a higher score and return a Viterbi path close to the original one, i.e., if the original Viterbi path is expanded by a frequency shift due to the Doppler modulation, the expanded path should intersect the new path returned when the Doppler modulation is turned off. Searching this final candidate with the Doppler modulation turned off yields a decreased Viterbi score 5.91 (cf. 7.12 in the original search). The newly returned Viterbi path differs from the original path by ~ 0.005 Hz ($< 10^{-4} f_0$). The two paths are considered overlapped when taking into consideration the frequency shift due to the Earth's orbit. The results for this candidate do not confidently show consistency with either an astrophysical signal or an outlier caused by noise artifacts. Therefore, while the candidate cannot be vetoed at this point, the possibility that it comes from astrophysical origin is low. Given the threshold chosen for $\alpha_f = 1\%$ per sub-band and the fact that the original score of the candidate is only slightly above this threshold ($S - S_{\text{th}} = 0.17$), the final candidate in sub-band 876–877 Hz could possibly be a false alarm. We provide the full Viterbi path of the final candidate in Appendix A and recommend following

it up in future observing runs, including the data already collected in the third observing run.

B. Strain upper limits

No strong evidence of continuous waves is found in this search. We place a frequentist upper limit on the signal strain at 95% confidence level, denoted by $h_0^{95\%}$, as a function of frequency through injections into the O2 data. Figure 5 shows $h_0^{95\%}$ in all 741 sub-bands where no candidate is vetoed (blue dots), as well as nine sample $h_0^{95\%}$ values obtained from injections (orange stars). The procedure of producing these results is as follows. First, we derive the upper limit in one sample sub-band, 715–716 Hz. A set of 100 synthetic signals are injected into the O2 data at the sky position of Fomalhaut b in that sub-band with a fixed h_0 . The other source parameters are randomly drawn from their uniform distributions. The corresponding detection rate is calculated. This process is repeated with different h_0 values with step size 1×10^{-27} until 95% of the injections are recovered. The $h_0^{95\%}$ value found in the sample sub-band is 1.67×10^{-25} (the same as described in Section III C). This value is then used to analytically calculate $h_0^{95\%}$ in the full frequency band (blue dots), using the scaling $h_0^{95\%}(f) \propto S_h^{1/2}(f)$. Here $S_h^{1/2}(f)$ is the effective ASD calculated from the harmonic mean of the two detectors over all the 30-min SFTs collected from GPS time 1180310418–1187733592. The sub-bands containing vetoed candidates, where no

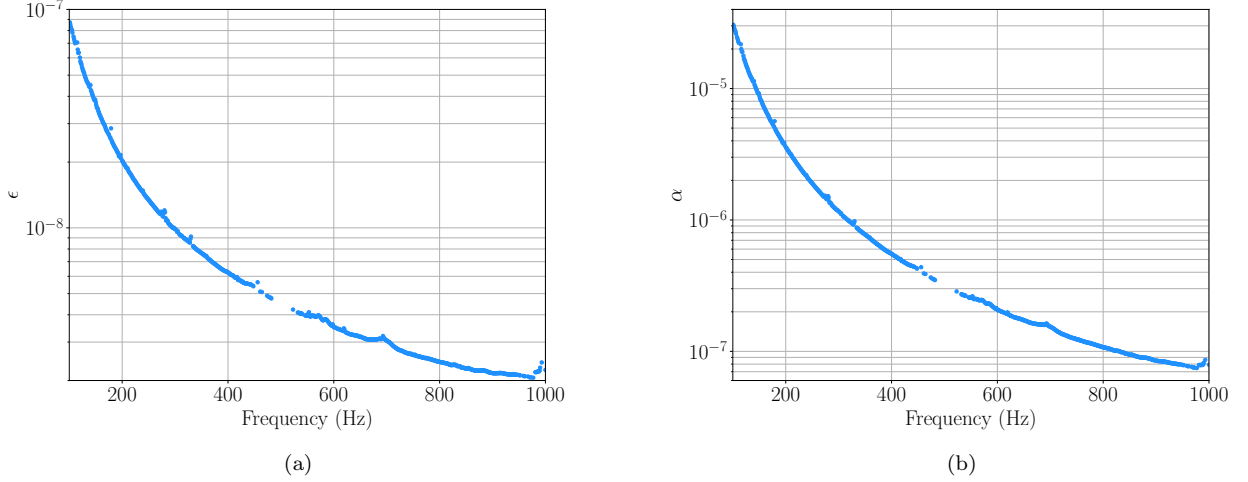


FIG. 6. Upper limits on (a) fiducial ellipticity ϵ and (b) r -mode amplitude α , converted from the strain upper limits in Figure 5.

upper limit can be placed, are excluded. Finally, in order to verify the analytical scaling, the simulation procedure in the first step is repeated in another eight sub-bands starting from 115 Hz, 165 Hz, 215 Hz, 365 Hz, 415 Hz, 565 Hz, 665 Hz, and 765 Hz. The $h_0^{95\%}$ values obtained empirically in those sub-bands (orange stars) generally agree with the analytic estimates.

The indirect upper limit on signal strain due to energy conservation, inferred from the age and distance of the source, is given by [12, 32]

$$h_0^{\text{age}} = 1.26 \times 10^{-24} \left(\frac{3.3 \text{ kpc}}{D} \right) \left(\frac{300 \text{ yr}}{t_{\text{age}}} \right)^{1/2}, \quad (22)$$

where D is the distance to the star. Assuming that Fomalhaut b is a neutron star with $t_{\text{age}} = 3000$ kyr and $D = 0.02$ kpc (the pessimistic scenario presented in Ref. [12]), we have $h_0^{\text{age}} = 2.08 \times 10^{-24}$. The upper limits obtained in this analysis beat the indirect limit h_0^{age} in the full band searched. We compare the strain upper limits obtained from this search to the previous results in Ref. [12]. In the most sensitive band around 200 Hz, $h_0^{95\%} = 1.2 \times 10^{-25}$ is obtained in Advanced LIGO's first observing run, as presented in Ref. [12]. In this search, the strain upper limit in the most sensitive 1-Hz sub-band starting from 194 Hz, $h_0^{95\%} = 9.19 \times 10^{-26}$, improves on previously published results by a factor of 1.3.

We then convert $h_0^{95\%}$ to the upper limits on the fiducial ellipticity of the neutron star [12, 32]

$$\epsilon = 9.5 \times 10^{-5} \left(\frac{h_0}{1.2 \times 10^{-24}} \right) \left(\frac{D}{1 \text{ kpc}} \right) \left(\frac{100 \text{ Hz}}{f} \right)^2, \quad (23)$$

and the r -mode amplitude parameter [12, 33, 34]

$$\alpha = 0.028 \left(\frac{h_0}{10^{-24}} \right) \left(\frac{D}{1 \text{ kpc}} \right) \left(\frac{100 \text{ Hz}}{f} \right)^3. \quad (24)$$

Figure 6 shows the upper limits on ϵ and α as a function of frequency, assuming a distance of $D = 0.011$ kpc, and the principal moment of inertia $I_{zz} = 10^{45} \text{ g cm}^2$.

V. CONCLUSION

We report the results from a directed search for CW signals from the neutron star candidate Fomalhaut b in the frequency band 100–1000 Hz, using Advanced LIGO O2 data. An efficient, semicoherent search method, based on a HMM tracking scheme and a matched filter \mathcal{F} -statistic, is used to track the signal frequency. After passing the above-threshold candidates through five veto steps, only one candidate survives. The final surviving candidate appears to be consistent with the false alarm probability, and no compelling evidence of continuous waves is found. Upper limits are placed on h_0 with 95% confidence in the full frequency band. In the most sensitive sub-band, 194–195 Hz, we obtain $h_0^{95\%} = 9.19 \times 10^{-26}$.

In the future, the search may benefit from new information gathered from electromagnetic observations of the source, as well as the further upgrading of the instruments. In particular, the final candidate in the sub-band 876–877 Hz can be followed up in the third observing run or future runs of Advanced LIGO and Virgo. Regardless of the eventual outcome of this search, this methodology represents an important development in the search for CWs and could easily be extended to other isolated neutron star sources.

VI. ACKNOWLEDGMENTS

This research has made use of data, software and/or web tools obtained from the Gravitational Wave Open Sci-

ence Center (<https://www.gw-openscience.org>), a service of LIGO Laboratory, the LIGO Scientific Collaboration and the Virgo Collaboration. LIGO is funded by the U.S. National Science Foundation. Virgo is funded by the French Centre National de Recherche Scientifique (CNRS), the Italian Istituto Nazionale della Fisica Nucleare (INFN) and the Dutch Nikhef, with contributions by Polish and Hungarian institutes. The authors would like to thank the LIGO Laboratory for providing the resources with which to conduct this search, as well as Alan Weinstein and the LIGO SURF program, the National Science Foundation, and the California Institute of Technology for sponsoring the project. The authors also would like to thank Meg Millhouse for the review and suggestions. L. Sun is a member of the LIGO Laboratory. LIGO was constructed by the California Institute of Technology and Massachusetts Institute of Technology

with funding from the United States National Science Foundation, and operates under cooperative agreement PHY-1764464. Advanced LIGO was built under award PHY-0823459. The authors would like to thank all of the essential workers who put their health at risk during the COVID-19 pandemic, without whom we would not have been able to complete this work. This paper carries LIGO Document Number LIGO-P2000118.

Appendix A: Viterbi path of the candidate in 876–877 Hz band

Here we provide the output Viterbi path for the final candidate surviving all vetoes in Section IV A. The frequencies at discrete time steps are listed in Table III and plotted in Figure 7.

-
- [1] B. P. Abbott *et al.* (LIGO Scientific Collaboration and Virgo Collaboration), “Observation of gravitational waves from a binary black hole merger,” *Phys. Rev. Lett.* **116**, 061102 (2016).
 - [2] J. Aasi *et al.* (LSC), “Advanced LIGO,” *Classical and Quantum Gravity* **32**, 074001 (2015).
 - [3] F. Acernese *et al.* (Virgo), “Advanced Virgo: a second-generation interferometric gravitational wave detector,” *Classical and Quantum Gravity* **32**, 024001 (2015).
 - [4] B. P. Abbott *et al.* (LIGO Scientific Collaboration and Virgo Collaboration), “GWTC-1: A Gravitational-Wave Transient Catalog of Compact Binary Mergers Observed by LIGO and Virgo during the First and Second Observing Runs,” *Phys. Rev. X* **9**, 031040 (2019).
 - [5] B. P. Abbott *et al.*, “GW190412: Observation of a Binary-Black-Hole Coalescence with Asymmetric Masses,” (2020), [arXiv:2004.08342 \[astro-ph.HE\]](https://arxiv.org/abs/2004.08342).
 - [6] B. P. Abbott *et al.*, “GW190425: Observation of a compact binary coalescence with total mass $\sim 3.4\,m_{\odot}$,” *The Astrophysical Journal* **892**, L3 (2020).
 - [7] R. Abbott *et al.*, “GW190814: Gravitational waves from the coalescence of a 23 solar mass black hole with a 2.6 solar mass compact object,” *The Astrophysical Journal Letters* **896**, L44 (2020).
 - [8] K. Riles, “Recent searches for continuous gravitational waves,” *Mod. Phys. Lett. A* **32**, 1730035 (2017).
 - [9] B. P. Abbott *et al.* (LIGO Scientific Collaboration and Virgo Collaboration), “Narrow-band search for gravitational waves from known pulsars using the second LIGO observing run,” *Phys. Rev. D* **99**, 122002 (2019).
 - [10] B. P. Abbott *et al.*, “Searches for gravitational waves from known pulsars at two harmonics in 2015–2017 LIGO data,” *The Astrophysical Journal* **879**, 10 (2019).
 - [11] B. P. Abbott *et al.*, “Search for gravitational waves from Scorpius X-1 in the second Advanced LIGO observing run with an improved hidden Markov model,” (2019), [arXiv:1906.12040 \[gr-qc\]](https://arxiv.org/abs/1906.12040).
 - [12] B. P. Abbott *et al.*, “Searches for Continuous Gravitational Waves from 15 Supernova Remnants and Fomalhaut b with Advanced LIGO,” *The Astrophysical Journal* **875**, 122 (2019).
 - [13] Lee Lindblom and Benjamin J. Owen, “Directed searches for continuous gravitational waves from twelve supernova remnants in data from advanced ligo’s second observing run,” *Phys. Rev. D* **101**, 083023 (2020).
 - [14] M. Millhouse, L. Strang, and A. Melatos, “Search for gravitational waves from twelve young supernova remnants with a hidden Markov model in Advanced LIGO’s second observing run,” (2020), [arXiv:2003.08588 \[gr-qc\]](https://arxiv.org/abs/2003.08588).
 - [15] B. P. Abbott *et al.* (LIGO Scientific Collaboration and Virgo Collaboration), “All-sky search for continuous gravitational waves from isolated neutron stars using Advanced LIGO O2 data,” *Phys. Rev. D* **100**, 024004 (2019).
 - [16] R. Abbott *et al.*, “Open data from the first and second observing runs of Advanced LIGO and Advanced Virgo,” (2019), [arXiv:1912.11716 \[gr-qc\]](https://arxiv.org/abs/1912.11716).
 - [17] T. Currie *et al.*, “Direct imaging confirmation and characterization of a dust-enshrouded candidate exoplanet orbiting Fomalhaut,” *The Astrophysical Journal* **760**, L32 (2012).
 - [18] Paul Kalas, James R. Graham, Eugene Chiang, Michael P. Fitzgerald, Mark Clampin, Edwin S. Kite, Karl Stapelfeldt, Christian Marois, and John Krist, “Optical images of an exosolar planet 25 light-years from earth,” *Science* **322**, 1345–1348 (2008).
 - [19] R. Neuhuser, M. M. Hohle, C. Ginski, J. G. Schmidt, V. V. Hambaryan, and T. O. B. Schmidt, “The companion candidate near Fomalhaut – a background neutron star?” *Monthly Notices of the Royal Astronomical Society* **448**, 376–389 (2015).
 - [20] Andrs Gspr and George H. Rieke, “New HST data and modeling reveal a massive planetesimal collision around Fomalhaut,” *Proceedings of the National Academy of Sciences* **117**, 97129722 (2020).
 - [21] G. Hobbs, A. G. Lyne, and M. Kramer, “An analysis of the timing irregularities for 366 pulsars,” *Monthly Notices of the Royal Astronomical Society* **402**, 1027–1048 (2010).
 - [22] L. Sun, A. Melatos, S. Suvorova, W. Moran, and R. J. Evans, “Hidden markov model tracking of continuous gravitational waves from young supernova remnants,” *Phys. Rev. D* **97**, 043013 (2018).

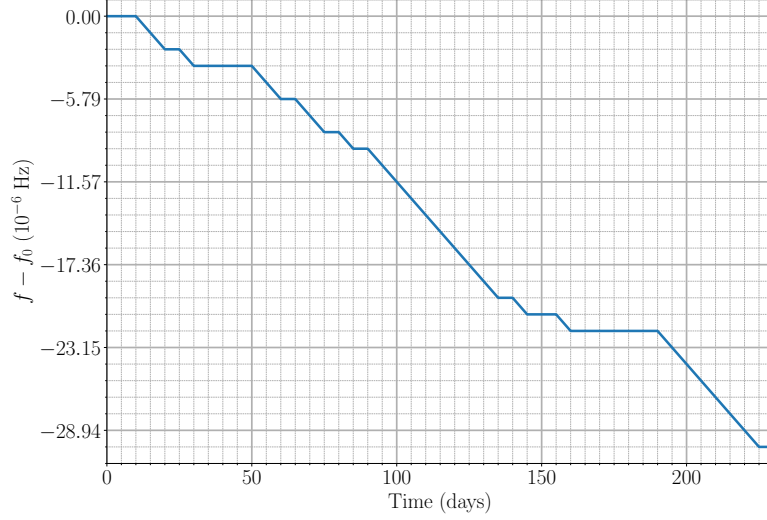


FIG. 7. Viterbi path of the final candidate surviving all vetoes in the sub-band 876–877 Hz. The starting frequency equals the frequency at the first step in Table III, $f_0 = 876.5034513780022$ Hz.

- [23] B. P. Abbott *et al.* (LIGO Scientific Collaboration and Virgo Collaboration), “Search for gravitational waves from Scorpius X-1 in the first Advanced LIGO observing run with a hidden Markov model,” *Phys. Rev. D* **95**, 122003 (2017).
- [24] Ling Sun and Andrew Melatos, “Application of hidden Markov model tracking to the search for long-duration transient gravitational waves from the remnant of the binary neutron star merger GW170817,” *Phys. Rev. D* **99**, 123003 (2019).
- [25] Ling Sun, Richard Brito, and Maximiliano Isi, “Search for ultralight bosons in cygnus x-1 with advanced ligo,” *Phys. Rev. D* **101**, 063020 (2020).
- [26] P. Jaranowski, A. Królak, and B. F. Schutz, “Data analysis of gravitational-wave signals from spinning neutron stars: The signal and its detection,” *Physical Review D* **58**, 063001 (1998).
- [27] R. Prix, “Search for continuous gravitational waves: Metric of the multidetector F-statistic,” *Physical Review D* **75**, 023004 (2007).
- [28] A. Viterbi, “Error bounds for convolutional codes and an asymptotically optimum decoding algorithm,” *IEEE Transactions on Information Theory* **13**, 260–269 (1967).
- [29] P. B. Covas *et al.* (LSC Instrument Authors), “Identification and mitigation of narrow spectral artifacts that degrade searches for persistent gravitational waves in the first two observing runs of advanced ligo,” *Phys. Rev. D* **97**, 082002 (2018).
- [30] “Gravitational Wave Open Science Center – O2 Instrumental Lines,” <https://www.gw-openscience.org/o2specclines/>.
- [31] Sylvia J. Zhu, Maria Alessandra Papa, and Sinéad Walsh, “New veto for continuous gravitational wave searches,” *Phys. Rev. D* **96**, 124007 (2017).
- [32] K Wette, B J Owen, B Allen, M Ashley, J Betzwieser, N Christensen, T D Creighton, V Dergachev, I Gholami, E Goetz, R Gustafson, D Hammer, D I Jones, B Krishnan, M Landry, B Machenschalk, D E McClelland, G Mendell, C J Messenger, M A Papa, P Patel, M Pitkin, H J Pletsch, R Prix, K Riles, L Sancho de la Jordana, S M Scott, A M Sintes, M Trias, J T Whelan, and G Woan, “Searching for gravitational waves from cassiopeia a with LIGO,” *Classical and Quantum Gravity* **25**, 235011 (2008).
- [33] Benjamin J. Owen, “How to adapt broad-band gravitational-wave searches for r -modes,” *Phys. Rev. D* **82**, 104002 (2010).
- [34] Lee Lindblom, Benjamin J. Owen, and Sharon M. Morsink, “Gravitational radiation instability in hot young neutron stars,” *Phys. Rev. Lett.* **80**, 4843–4846 (1998).

Step	Frequency (Hz)
1	876.5034513780022
2	876.5034513780022
3	876.5034513780022
4	876.5034502205948
5	876.5034490631874
6	876.5034490631874
7	876.5034479057800
8	876.5034479057800
9	876.5034479057800
10	876.5034479057800
11	876.5034479057800
12	876.5034467483727
13	876.5034455909653
14	876.5034455909653
15	876.5034444335579
16	876.5034432761505
17	876.5034432761505
18	876.5034421187431
19	876.5034421187431
20	876.5034409613357
21	876.5034398039284
22	876.5034386465210
23	876.5034374891136
24	876.5034363317062
25	876.5034351742988
26	876.5034340168914
27	876.5034328594841
28	876.5034317020767
29	876.5034317020767
30	876.5034305446693
31	876.5034305446693
32	876.5034305446693
33	876.5034293872619
34	876.5034293872619
35	876.5034293872619
36	876.5034293872619
37	876.5034293872619
38	876.5034293872619
39	876.5034293872619
40	876.5034282298545
41	876.5034270724472
42	876.5034259150398
43	876.5034247576324
44	876.5034236002250
45	876.5034224428176
46	876.5034212854102
47	876.5034212854102

TABLE III. Frequencies at each step on the candidate Viterbi path.